ACS APPLIED MATERIALS & INTERFACES

Research Article

Cite This: ACS Appl. Mater. Interfaces 2019, 11, 26976−26984

www.acsami.org

SnP_3/Carbon Nanocomposite as an Anode Material for Potassium-Ion Batteries

Rakesh Verma,[†] Pravin N. Didwal,[†] Hyeong-Seo Ki,[†] Guozhong Cao,*[,‡] and Chan-Jin Park*[,†]

[†]Department of Materials Science and Engineering, Chonnam National University, 77, Yongbongro, Bukgu, Gwangju 61186, South Korea

[‡]Department of Materials Science and Engineering, University of Washington, Seattle, Washington 98195, United States

Supporting Information

ABSTRACT: New anode materials with large capacity and long cyclability for next-generation potassium-ion batteries (PIBs) are required. PIBs are in the initial stage of investigation and only a few anode materials have been explored. In this study, for the first time, an SnP_3/C nanocomposite with superior cyclability and rate performance was evaluated as an anode for PIBs. The SnP_3/C nanocomposite was synthesized by a facile and cost-effective high-energy ball-milling technique. The SnP_3/C electrode delivered a first reversible capacity of 410 mAh g^{-1} and maintained 408 mAh g^{-1} after 50 cycles at a specific current of 50 mA g^{-1}. After 80 cycles at a high specific current of 500 mA g^{-1}, a high capacity of 225 mAh g^{-1} remained. From a crystallographic analysis, it was suggested that the SnP_3/C nanocomposite underwent a sequential and reversible conversion and alloying reactions. The excellent cycling stability and rate capability of the SnP_3/C electrode were attributed to the nanosized SnP_3 particles and carbon buffer layer, which supplied channels for the migration of K-ions and mitigated the stress induced by a large volume change during potassiation/depotassiation. In addition, a full cell composed of the SnP_3/C nanocomposite anode and potassium Prussian blue cathode exhibited a reversible capacity of 305 mAh g^{-1} at a specific current of 30 mA g^{-1} and retained 71.7% of the original capacity after 30 cycles. These results are important for understanding the electrochemical process of the SnP_3/C nanocomposite and using the SnP_3/C as an anode for PIBs.

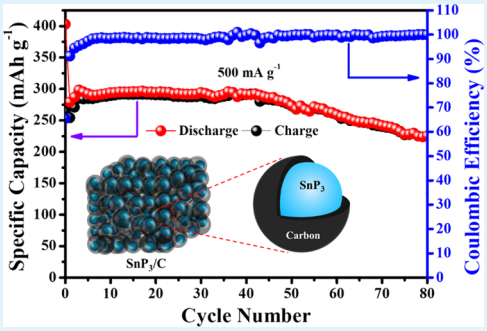

KEYWORDS: *potassium-ion batteries, SnP_3 nanocomposites, cyclability, rate performance, full cells*

INTRODUCTION

Recently, potassium-ion batteries (PIBs) are drawing much attention in the research community as a promising alternative to conventional lithium-ion batteries for large-scale energy storage systems (ESSs) owing to their inexpensive and abundant resources.[1−4] As compared to sodium-ion batteries (SIBs), PIBs could provide a higher cell potential and faster kinetics owing to the lower redox potential of K^+/K and the weaker solvation effect of K^+, respectively.[3,5] In particular, scientific research on PIB electrode materials is less limited than that on SIBs. However, because of the larger radius of the K^+ (1.38 Å) than that of Na^+ (1.02 Å) and Li^+ (0.76 Å), suitable electrode materials that enable repeated potassiation and depotassiation to achieve high cycling stability are difficult to develop.[6,7] Therefore, the design and fabrication of suitable PIB electrode having higher capacity and cyclability is of immense importance.[8]

Over the past several years, studies have focused mainly on the development of electrode materials for PIBs. For the cathode materials, Prussian blue and analogues,[8−11] $KVOPO_4$,[12] $FeSO_4F$,[13] $K_{0.3}MnO_2$,[14] K_xCoO_2,[15] $K_{0.6}CoO_2$,[16] $K_3V_2(PO_4)_3$,[17] amorphous $FePO_4$,[18] $K_{0.65}Fe_{0.5}Mn_{0.5}O_2$,[19] and organic perylene−tetracarboxylic acid−dianhydride[20] have been investigated. For the anode materials, recent studies have focused on carbonaceous materials due to their low cost and high electrical conductivity.[21] Nevertheless, the capacities of carbonaceous materials (≤273 mAh g^{-1}) cannot satisfy the requirements for practical applications, such as ESSs. Recently, alloy-type anode materials look impressive because of their appropriate electrode potentials and high theoretical-specific capacities.[22] The binary-phase diagram reveals that potassium can be alloyed with some metallic elements at room temperature that form intermetallic compounds.[23,24] A few studies on alloy-type anode materials, such as phosphorus-based composites,[25,26] Sn-based composites,[24,27] and porous Bi-[28] and Sb-based composites,[29] have been reported for PIB applications. The Sn/C composite displayed a first discharge capacity of approximately 290 mAh g^{-1} and maintained a reversible capacity of 110 mAh g^{-1} after 30 cycles at a specific current of 25 mA g^{-1}.[27] Furthermore, the three-dimensional (3D) Sn/C composite suggested by Ju et al. exhibited a first discharge capacity of 848 mAh g^{-1} and maintained a high reversible capacity of 276.4 mAh g^{-1} at a specific current of 50 mA g^{-1} after 100 cycles.[24] Qian et al. prepared an Sb/graphene

Received: May 9, 2019
Accepted: June 28, 2019
Published: June 28, 2019

DOI: 10.1021/acsami.9b08088
ACS Appl. Mater. Interfaces 2019, 11, 26976−26984

Scheme 1. Schematic of the Synthesis Process for the SnP_3/C Nanocomposite

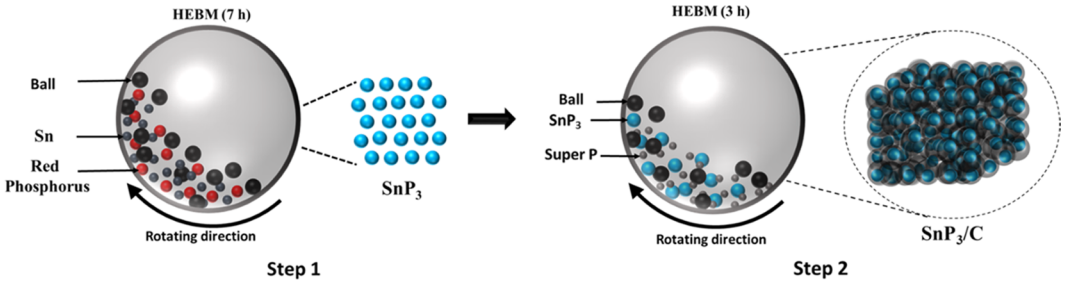

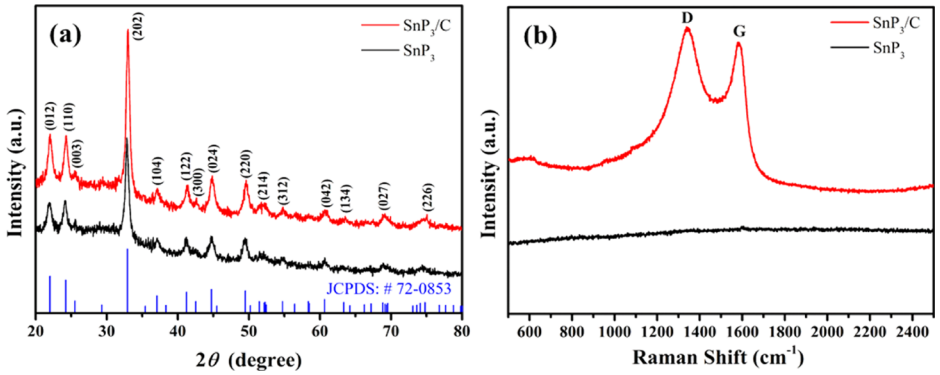

Figure 1. (a) XRD patterns and (b) Raman spectra of the SnP_3/C nanocomposite and pristine SnP_3.

composite via a molten-salt route, which delivered the initial discharge capacity of approximately 610 mAh g^{-1} and maintained a reversible capacity of 210 mAh g^{-1} at 500 mA g^{-1} after 200 cycles.[29] Among several alloy-type materials, Sn−P compounds are potential candidates because they have the highest theoretical capacity among the reported anodes. Recently, Guo et al. synthesized an Sn_4P_3/C composite via a ball-milling technique.[22] The Sn_4P_3/C composite delivered the first discharge capacity of 588 mAh g^{-1} and retained a reversible capacity of 384.8 mAh g^{-1} after 50 cycles at a specific current of 50 mA g^{-1}.

Various routes for the synthesis of Sn−P compounds, such as high-energy ball milling,[30] hydrothermal route,[31] and solid-state route,[32] have been reported. Tin phosphide synthesized via a hydrothermal route delivered an excellent electrochemical performance.[31] However, the complicated synthesis process along with the presence of impure phases confronts several questions on the industrial visibility of this process. High-temperature processing, via solid-state synthesis, inevitably makes white phosphorus, which is chemically unstable at room temperature and restrain its viability.[32] In contrast, the ball-milling technique is most impressive in terms of the mass production of high-purity Sn−P-based materials. Therefore, in this study, SnP_3 and SnP_3/C were synthesized via a facile, scalable, and cost-effective high-energy ball-milling (HEBM) technique.

This study shed light for the first time on the use of SnP_3 as a potential anode for PIBs. The electrochemical performance of pure SnP_3 is unacceptable owing to the degradation of the electrodes caused by a large volume change during the potassiation and depotassiation processes. The use of the SnP_3/C composite is the easiest way to address this issue. The nanostructure of SnP_3 with a particle size of approximately 20 nm enclosed by an amorphous carbon could improve the performance of SnP_3. Herein, the cyclability and low Coulombic efficiency of the SnP_3 electrode induced by the pulverization and contact loss during the discharge−charge process have been successfully addressed.

RESULTS AND DISCUSSION

SnP_3 nanoparticles interconnected by an amorphous carbon were made using a simple and cost-effective high-energy ball-milling (HEBM) technique, as shown in Scheme 1. The process was composed of a two-step ball milling: (1) the metallic Sn reacted with red phosphorus for 7 h to form the SnP_3 nanoparticles and then (2) 20 wt % super P was mixed with the SnP_3 nanoparticles for 3 h to form the SnP_3/C nanocomposite. The amorphous carbon was adhered to the SnP_3 nanoparticles after ball milling, enabling facile electron transfer and stabilizing the solid electrolyte interphase (SEI) layer on the surface. For a comparison, pristine SnP_3 was also prepared without the second ball-milling step. The X-ray diffraction (XRD) peaks of the synthesized SnP_3/C composite and pristine SnP_3 are shown in Figure 1a. All of the characteristic peaks of the SnP_3/C and SnP_3 samples could be assigned to the pure SnP_3 phase (JCPDS#72-0853, space group, *R*3*m*) with the rhombohedral crystal structure. In both samples, peaks associated with the impurity phases were not observed. After the second ball-milling step for the synthesis of SnP_3/C, a little broadening in the diffraction peaks was found, indicating the nanocrystalline nature of the SnP_3/C composite. The calculated lattice parameters were a = 7.365 Å, b = 7.365 Å, c = 10.502 Å, $\alpha = \beta = 90°$, and $\gamma = 120°$ for the SnP_3/C nanocomposite. The average crystallite sizes of the SnP_3/C nanocomposite and pristine SnP_3 were approximately 20 and 35 nm, respectively, using the Scherrer equation for an estimation. In addition, from the Raman spectrum (Figure 1b), the appearance of two peaks at ∼1344 and 1586 cm^{-1} is ascribed to the disorder-induced D band and graphitic G band of carbon, respectively. The I_D/I_G ratio was 1.08, indicating the

DOI: 10.1021/acsami.9b08088
ACS Appl. Mater. Interfaces 2019, 11, 26976−26984

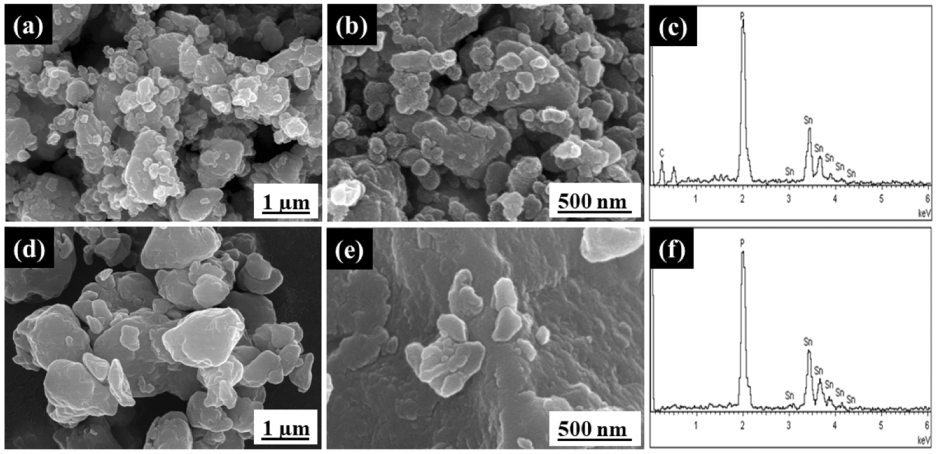

Figure 2. (a) Low- and (b) high-magnification SEM images and the corresponding (c) EDS spectra of the SnP_3/C nanocomposite. Images (d) and (e) show the low- and high-magnification SEM images, respectively, and the corresponding (f) EDS spectra of pristine SnP_3.

highly disordered nature of carbon in the SnP_3/C nanocomposite.

Scanning electron microscopy (SEM) is used to investigate the morphologies of the SnP_3/C nanocomposite and pristine SnP_3, as displayed in Figure 2. The SnP_3/C consisted of irregular agglomerated nanosized particles, as shown in Figure 2a,b. Each agglomerated SnP_3/C particle was composed of numerous crystalline nanoparticles with a size of approximately 10−20 nm. The pristine SnP_3 sample exhibited a similar irregular morphology as that of the SnP_3/C nanocomposite. However, the average size of the pristine SnP_3 particles was larger, which could be attributed to the shorter ball-milling time. From the energy-dispersive X-ray spectroscopy (EDS) analysis, the molar ratio of Sn to P was approximately 1:3 close to the designed composition in the SnP_3/C and SnP_3 samples. Further, after combining with super P carbon by the second HEBM, there was a significant morphology change in the SnP_3/C composite, as evidenced by the SEM and transmission electron microscopy (TEM) micrographs. These changes in the morphology are advantageous in two ways. First, compared with pristine SnP_3, the primary particle size of SnP_3/C further decreased to nanometer range and the primary particles were densely aggregated into microsized particles (Figure 3a) due to the high surface energy of nanoparticles. This unique change in the morphology can facilitate electrolyte infiltration, shorten the diffusion distance of K-ions, and reduce structural stress. Second, the presence of carbon in the composite not only minimizes the agglomerations but also buffers the volume expansion. This also facilitates the electron transfer and stabilizes the solid electrolyte interphase (SEI) layer on the surface compared with those of pristine SnP_3. As a result, there is not only an increase in the electrode tap density leading to the increase in the volumetric energy density but also an enhancement in the initial cycle Coulombic efficiency by reducing the side reactions at the electrode/electrolyte interface.

The microstructure of the SnP_3/C composite was further examined by transmission electron microscopy (TEM), as shown in Figure 3. The SnP_3 nanoparticles were homogeneously enclosed by the amorphous carbon matrix (Figure 3a,b), which could improve the ionic and electronic conductivities. The amorphous carbon coating can provide a buffer layer to accommodate the volume change and mechanical stress induced during potassiation and depotassiation. High-resolution TEM was used to analyze the microstructure of SnP_3 nanoparticles. The lattice spacing of 0.405 and 0.367 nm corresponding to the (012) and (110) planes, respectively, was measured (Figure 3b). The selected area diffraction pattern (Figure 3c) showed the well-crystallized SnP_3, where the ring patterns were assigned to the (110), (012), (101), and (003) planes of SnP_3. Figure 3d−g shows the EDS elemental mapping of the SnP_3 nanoparticles, confirming the homogeneous distributions of Sn, phosphorus, and carbon.

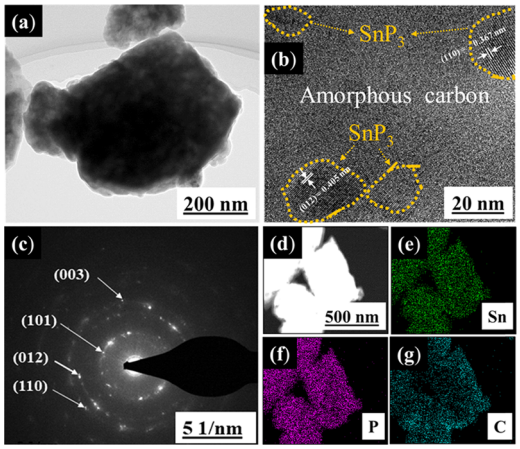

Figure 3. TEM analyses of the prepared SnP_3/C nanocomposite: (a) TEM images, (b) high-resolution (HR)-TEM image with yellow outlines indicating the SnP_3 nanoparticles, (c) selected area electron diffraction pattern, (d) scanning TEM image, and the corresponding EDS elemental mappings of (e) Sn, (f) P, and (g) C.

X-ray photoelectron spectroscopy (XPS) was used to examine the surface chemical state of the SnP_3/C nanocomposite, as shown in Figure 4. The XPS survey spectra of the SnP_3/C nanocomposite displayed distinct peaks corresponding to P 2p, C 1s, Sn $3d_{5/2}$, Sn $3d_{3/2}$, and O 1s centered at 137.7, 284.1, 487.8, 495.6, and 532.5 eV, respectively (Figure 4a). The high-resolution XPS core spectrum of Sn 3d showed four deconvoluted peaks corresponding to Sn $3d_{5/2}$ at 485.5 and 487.8 eV and Sn $3d_{3/2}$ at 494 and 496.1 eV (Figure 4b). The smaller peaks at 485.5 and 494 eV corresponded to Sn^{3+}. The larger peaks at 487.2 and 496.1 eV originated from the oxidized Sn^{4+} on the surface of the nanoparticles.[33] High

DOI: 10.1021/acsami.9b08088
ACS Appl. Mater. Interfaces 2019, 11, 26976−26984

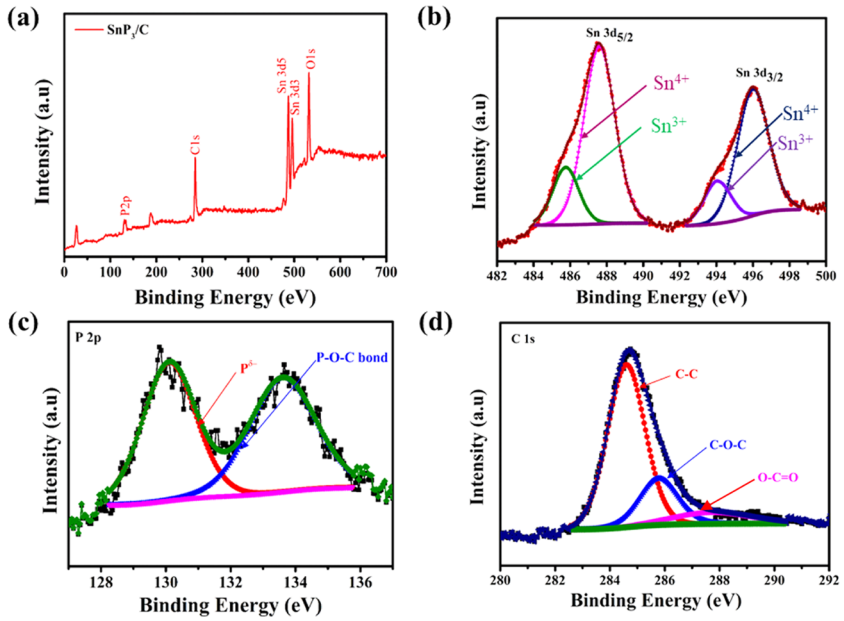

Figure 4. XPS analysis of the SnP_3/C nanocomposite: (a) XPS survey spectrum and XPS core spectra corresponding to (b) Sn 3d, (c) P 2p, and (d) C 1s.

oxidation occurred owing to the P surface termination, creating a higher Sn oxidation state. Some surface oxidation may be unavoidable, which is consistent with the peaks corresponding to the P−O bonds in the P 2p spectrum. This phenomenon was also confirmed in previous studies on other Sn−P compounds.[34,35] The P−O−C bond was present in the SnP_3/C nanocomposite, which was induced by strong mechanical milling, as shown in Figure 4c. This was also shown in other phosphorus/or metal phosphide/carbon systems.[36,37] The peak observed at 130.1 eV corresponded to elemental phosphorus, and another peak at 133.6 eV could be assigned to the oxidized P species.[33] The C 1s XPS core spectrum of the SnP_3/C nanocomposite is shown in Figure 4d. The spectra of the C 1s peak could be fitted into three components, centered at 284.6, 285.8, and 288.4 eV, corresponding to C−C, C−O−C, and C−C═O, respectively.[24,38,39]

To measure the specific surface area of the synthesized SnP_3/C and SnP_3, N_2 adsorption−desorption isotherms of SnP_3/C and SnP_3 were performed, as shown in Figure S1. Using the Brunauer−Emmett−Teller (BET) and Barrett−Joyner−Halenda methods, the surface area, average pore diameter, and pore volume of the SnP_3/C sample were calculated to be 3.5 $m^2\ g^{-1}$, 35 nm, and 0.026 $cm^3\ g^{-1}$, respectively. Conversely, the pristine SnP_3 sample has a specific area of 2.1 $m^2\ g^{-1}$, an average pore diameter of 39 nm, and a pore volume of 0.019 $cm^3\ g^{-1}$, demonstrating a smaller surface area and porosity than those of the SnP_3/C sample.

The electrochemical properties of the SnP_3/C electrode were investigated using a 2032 coin-type cell, in which the SnP_3/C electrode was the working electrode and K-metal was the counter/reference electrode. Figure 5a shows the cyclic voltammograms for the SnP_3/C electrode, measured for the first five cycles in a potential range of 0.01−2 V vs K^+/K at a scan rate of 0.1 mV s^{-1}. The SnP_3/C electrode exhibited low potentials for potassiation and depotassiation, below approximately 0.8 V vs K^+/K. A large cathodic current was observed owing to the conversion followed by alloying reactions and the SEI formation in the first cathodic scan. One oxidation peak corresponding to depotassiation was centered at approximately 0.88 V vs K^+/K. The cyclic voltammograms for the electrode nearly overlapped from the second cycle to the following cycles. This suggested that the potassiation/depotassiation behavior was stable and reversible for the SnP_3/C nanocomposite electrode.

Figure 5b shows the galvanostatic discharge−charge curves of the SnP_3/C electrode, measured in a potential range of 0.01−2.0 V vs K^+/K at a specific current of 50 mA g^{-1}. The first discharge and charge capacities of the SnP_3/C electrode were 697 and 410 mAh g^{-1}, respectively, corresponding to an initial Coulombic efficiency of 58.8%. Based on previous studies, the initial large irreversible capacity was due to the formation of the SEI layer on the electrode surface.[40,41] The Coulombic efficiency became higher with an increase in the cycle number, indicating stabilization of the SEI layer while cycling. The Coulombic efficiency sharply increased to >93% in the second cycle. After 50 cycles, the SnP_3/C electrode maintained a capacity of 408 mAh g^{-1}, corresponding to the Coulombic efficiency close to 100%. For comparison, the discharge and charge profiles of pristine SnP_3 without a carbon coating are shown in Figure S2. The first discharge capacity and charge capacity of the pristine SnP_3 electrode were 906.8 and 402.9 mAh g^{-1}, respectively, corresponding to an initial Coulombic efficiency of 44.4%, which is less than that of the SnP_3/C electrode (58.8%).

In addition, the SnP_3/C and SnP_3 electrodes are shown in Figure 5c. A highly stable cycling performance was observed for the SnP_3/C electrode, while dramatic capacity fading was found for the pristine SnP_3 electrode. The capacity of the SnP_3/C electrode increased gradually to the 34th cycle and then decreased gradually. To determine the reason for this capacity fading, the change in the surface morphology of the electrode with the cycle was monitored using SEM, as shown in Figure S3. Several thin cracks were found on the surface of the electrode after 35 cycles, and the cracks were thickened after 50 cycles. These surface cracks were because of fatigue

DOI: 10.1021/acsami.9b08088
ACS Appl. Mater. Interfaces 2019, 11, 26976−26984

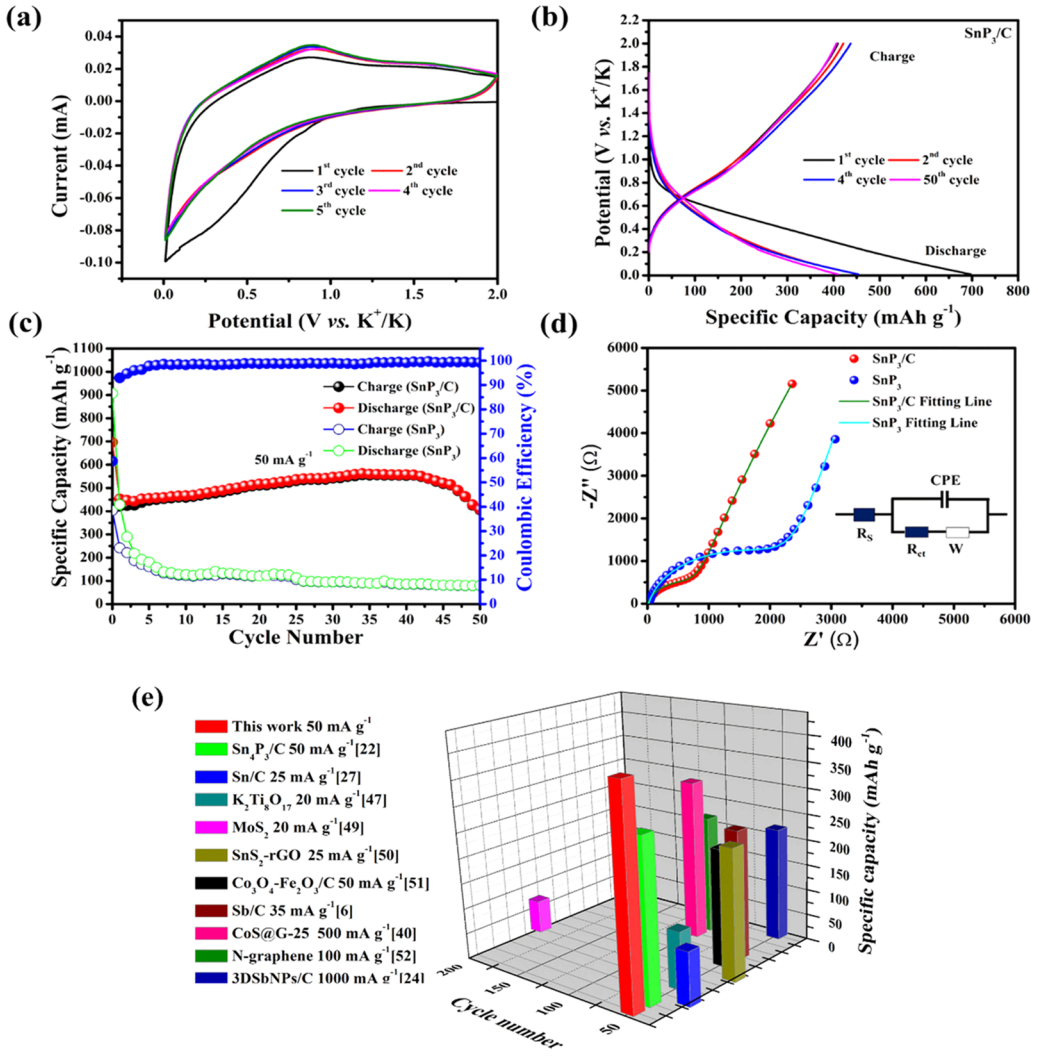

Figure 5. (a) Cyclic voltammograms of SnP_3/C corresponding to the first five cycles at a scan rate of 0.1 mV s^{-1}. (b) Selected discharge−charge potential profiles of SnP_3/C at a specific current of 50 mA g^{-1}. (c) Cycling performance of SnP_3/C and SnP_3. (d) Electrochemical impedance spectra (EIS) of SnP_3/C and SnP_3 measured before the cycling tests; the inset is the equivalent circuit used. (e) Comparison of SnP_3/C with the materials used in previous studies in terms of capacity and cyclability.

induced by the repeated volume change resulting from repeated potassiation/depotassiation. However, the SnP_3/C electrode maintained a reversible capacity of 408 mAh g^{-1} after 50 cycles. The improved capacity and cyclability of the SnP_3/C electrode were attributed to the presence of the carbon buffer layer, which provided a conductive network throughout the electrode and accommodated for the stress induced by the large volume change. Electrochemical impedance spectroscopy (EIS) curves of the SnP_3/C and SnP_3 electrodes before the cycling tests were compared, as shown in Figure 5d. The EIS curves could be well fitted using a simple Randles circuit. The EIS curves showed that the charge-transfer resistance (R_{ct}) of the SnP_3/C electrode was smaller than that of the SnP_3 electrode. This result indicated that the 20 wt % carbon was tightly bonded to the SnP_3 nanoparticles after ball milling, facilitating the electron transfer between the electrode and electrolyte. The initial reversible capacity and cyclability of the SnP_3/C electrode were compared with the previously reported anode materials, as shown in Figure 5e. This SnP_3/C nanocomposite showed the best electrochemical properties among the reported anode materials.

In addition to the cycling performance, the SnP_3/C electrode exhibited an excellent rate capability. The corresponding initial discharge−charge potential profile of SnP_3/C at various specific currents is shown in Figure 6a. The reversible initial charge capacities of 410, 405, 370, 324, 288, 248, and 212 mAh g^{-1} were observed at specific currents of 50, 100, 200, 300, 500, 800, and 1200 mA g^{-1}, respectively. As shown in Figure 6b, the discharge capacity decreased from 453.7 to 221.8 mAh g^{-1} when a specific current increased 24 times from 50 to 1200 mA g^{-1}. At the high specific current of 500 mA g^{-1}, the SnP_3/C electrode provided a reversible capacity of approximately 225 mAh g^{-1} even after 80 cycles, representing the best-reported data for PIB anode materials (Figure 6c). Furthermore, selected discharge−charge potential profiles and long-term cycling performance of SnP_3/C nanocomposite electrode for 200 cycles at a high specific capacity of 500 mAh g^{-1} are presented in Figure S4. However, the reversible capacity gradually decreased with further increase in the cycle at such a high specific capacity, indicating the gradual degradation of the electrode due to the limitation of interfacial kinetics. In Figure 6d, the rate capability of the SnP_3/C electrode was compared with that of other reported

DOI: 10.1021/acsami.9b08088
ACS Appl. Mater. Interfaces 2019, 11, 26976−26984

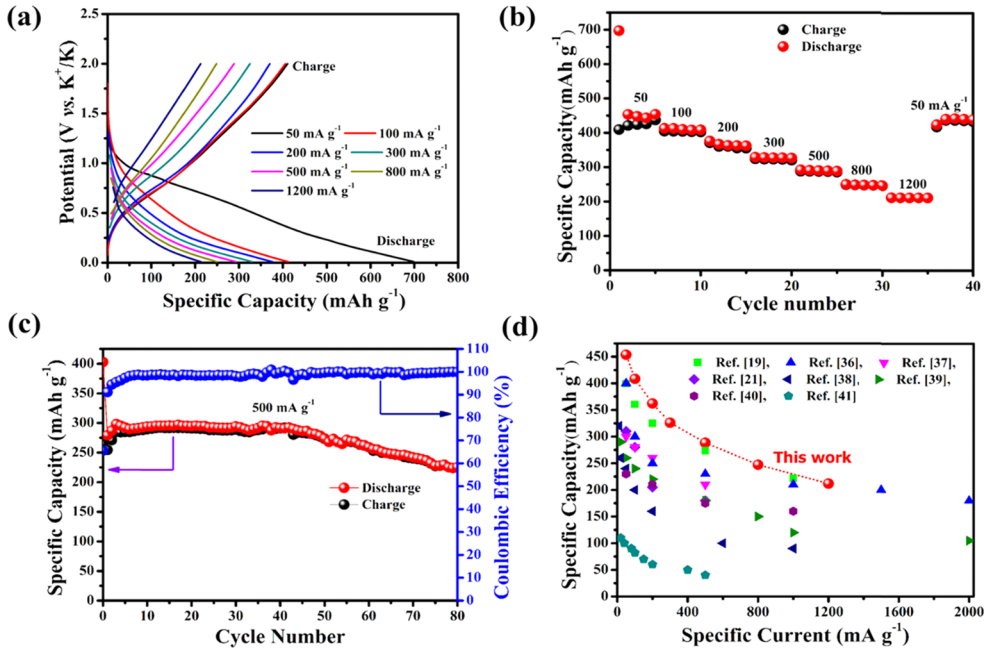

Figure 6. (a) Selected initial discharge−charge potential profiles of SnP_3/C at various specific currents. (b) Rate capability of the SnP_3/C electrode obtained by varying the specific current from 50 to 1200 mA g^{-1}. (c) Cyclability of SnP_3/C at a high specific current of 500 mA g^{-1}. (d) Comparison of SnP_3/C with the materials used in previous studies in terms of rate capability.

anode materials, such as Sn_4P_3/C,[22] N-doped porous carbon nanosheets,[42] N-doped porous carbon,[43] 3D hierarchically porous carbon/Sn composites,[24] N-doped carbon nanotubes,[44] N-doped cup-stacked carbon nanotubes,[45] S- and O-codoped porous hard carbon microspheres,[46] $K_2Ti_8O_{17}$,[47] etc. Figure 6d shows that the rate capability of the SnP_3/C electrode was superior to that of the reported anode materials.

To further understand the possible reaction mechanisms during the first discharge processes, the first discharged electrode was analyzed using XRD, as shown in Figure S5. After the first discharge to 0.01 V vs K^+/K, K_4Sn_{23} (JCPDS no. 065-3351), KSn (JCPDS no. 065-7670), and Sn (JCPDS no. 001-0926) phases were observed. The appearance of these phases indicated a conversion reaction followed by an alloying process. The suggested potassiation and depotassiation processes are as follows.[22]

$$SnP_3 + 9K^+ + 9e^- \leftrightarrow Sn + 3K_3P \quad (1)$$

$$23Sn + 4K^+ + 4e^- \leftrightarrow K_4Sn_{23} \quad (2)$$

$$K_4Sn_{23} + 19K^+ + 19e^- \leftrightarrow 23KSn \quad (3)$$

Scheme 2 shows the overall reaction stages for potassiation and depotassiation of the SnP_3/C nanocomposite. In the beginning stage of potassiation, a conversion reaction occurred, where the SnP_3 structure was converted into metallic Sn particles and a K_3P matrix (reaction 1). During the potassiation process, K^+ is alloyed with Sn to form the K_4Sn_{23} phase (reaction 2) followed by the formation of the KSn phase (reaction 3). During the depotassiation process, KSn is dealloyed into Sn and K^+, and then the Sn reacts with K_3P to convert to the original SnP_3. However, the K_3P phase could not be detected by ex situ XRD owing to the amorphous phase.[22,48] The K_3P phase formed after the conversion reaction could act as a kind of buffer material to mitigate the stress by the volume change during the cycling process.[22,48] In addition, the amorphous carbon matrix

Scheme 2. Potassiation and Depotassiation Processes in the SnP_3/C Nanocomposite Electrode

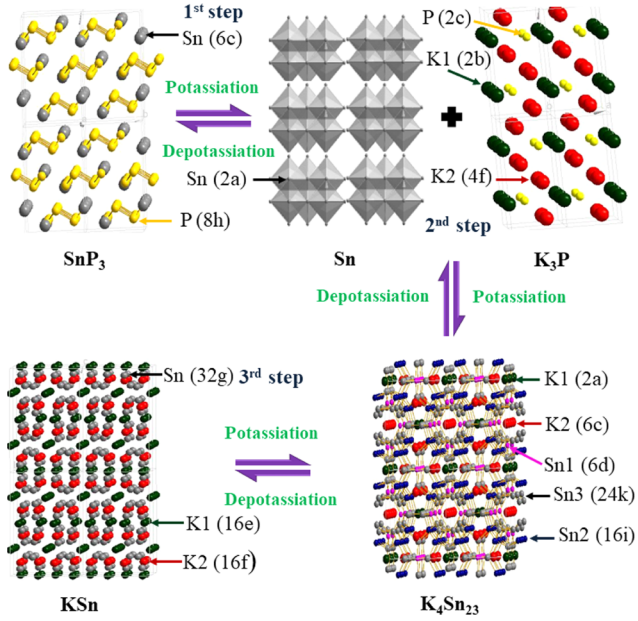

provided an additional buffering effect against the volume changes during potassiation and depotassiation. These buffering effects could maintain the integrity of the electrode, thus improving the cycling stability of the electrode. Furthermore, the formation of the K_4Sn_{23} and K_3P phases was ascertained by identifying their unique spacing in high-resolution HR-TEM images shown in Figure S6. The interlayer spacings of 0.245 and 0.284 nm are related to (422) and (110) planes of K_4Sn_{23} (JCPDS no. 065-3351) and K_3P phases (JCPDS no. 074-0128), respectively.

The potassiation and depotassiation mechanisms were also confirmed using XPS, as depicted in Figure S7. Figure S7a

DOI: 10.1021/acsami.9b08088
ACS Appl. Mater. Interfaces 2019, 11, 26976−26984

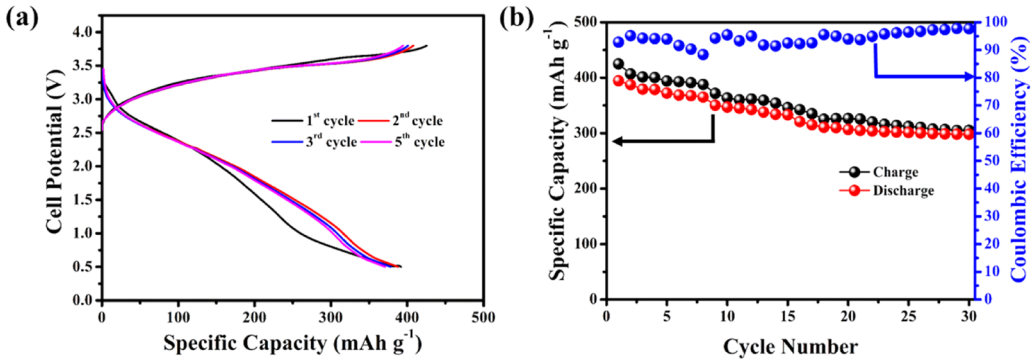

Figure 7. (a) Charge−discharge profiles and (b) cyclability of the full cell composed of the SnP_3/C anode and potassium Prussian blue cathode, measured at a specific current of 30 mA g^{-1}.

shows the full-survey spectrum of the SnP_3/C nanocomposite electrode after the first discharge to 0.01 V, which was composed of Sn, P, C, K, and O spectra. The high-resolution XPS spectrum of Sn 3d (Figure S7b) showed two deconvoluted peaks related to Sn $3d_{3/2}$ and Sn $3d_{5/2}$ at the binding energies of 494.5 and 485.8 eV, respectively, which corresponded to metallic Sn^0.[24] The spectrum of K 2p (Figure S7c) was characterized by two peaks with energy levels of K $2p_{3/2}$ and K $2p_{1/2}$ at 292.6 and 295.3 eV, respectively. In addition, in the P 2p spectrum, two types of phosphorus (Figure S7d) were revealed by XPS spectra. The peaks observed at 136.2 and 132.3 eV correspond to the phosphate species and phosphide, respectively.

Based on the advantages of the SnP_3/C nanocomposite discussed above, a full cell employing the SnP_3/C nanocomposite as an anode and potassium Prussian blue ($KFe_2(CN_6)$) as a cathode was produced and tested to demonstrate the applicability of the SnP_3/C nanocomposite anode in PIBs. The potassium Prussian blue was prepared according to a previous study.[9] Figure S8 depicts the XPD pattern of the potassium Prussian blue. The full cell was cyclic-tested at a specific current of 30 mA g^{-1} in a cell potential range of 0.5−3.8 V. Before the cell assembly, the Sn_3P/C anode was prepotassiated separately by coupling with K-metal to make a stable SEI layer and remove the side reaction effect. This strategy can minimize charge loss during the subsequent cycle and improve the Coulombic efficiency of the cell.[53] The first-cycle charge and discharge capacities of the full cell are 425 and 394 mAh g^{-1} with an impressive Coulombic efficiency of 92.7%, as depicted in Figure 7a. These capacities were smaller than those recorded from the half-cell, owing to the capacity balance issues between the anode and cathode and the system optimization. The cyclic performance of the cell is shown in Figure 7b. After 30 cycles, the reversible capacity of 305 mAh g^{-1} was maintained with a Coulombic efficiency of approximately 98%. The Coulombic efficiency and cyclability of the full cell should be improved further through a more detailed study of the whole system, including the cathode and electrolyte.

CONCLUSIONS

For the first time, the electrochemical properties of an SnP_3/C nanocomposite anode for PIBs were evaluated. The SnP_3/C nanocomposite was synthesized by a facile high-energy ball-milling technique. The SnP_3/C nanocomposite could reversibly react with K^+ through conversion and alloying reactions. The SnP_3/C nanocomposite exhibited a high initial reversible capacity of 410 mAh g^{-1} and retained 408 mAh g^{-1} after 50 cycles at 50 mA g^{-1}. A superior cyclability was demonstrated. At a high specific current of 500 mA g^{-1}, the electrode maintained a capacity of 225 mAh g^{-1} after 80 cycles, which was higher than carbon-based materials. In addition, the SnP_3/C electrode displayed an excellent rate capability by maintaining a specific capacity of 212 mAh g^{-1} at a high specific current of 1200 mA g^{-1}. The excellent electrochemical performance of the SnP_3/C electrode was attributed to the contributions of the nanosized SnP_3 particles and carbon buffer layer, which supplied channels for the migration of K-ions and mitigated the stress induced by the large volume change during the discharge−charge process. Furthermore, a full cell composed of the SnP_3/C nanocomposite anode and potassium Prussian blue cathode maintained a superior reversible capacity of 305 mAh g^{-1}, which corresponds to a capacity retention of 71.7% after 30 cycles at a specific current of 30 mAh g^{-1}. The SnP_3/C nanocomposite could be a promising anode for next-generation PIBs, based on its excellent K-ion storage characteristics.

EXPERIMENTAL SECTION

Material Synthesis. Pristine SnP_3 powder was synthesized using a high-energy ball-milling technique under an Ar atmosphere. Stoichiometric amounts of Sn metal (Sigma-Aldrich 99.99%) powders were mixed with red phosphorus (Alfa Aesar 98.99%) and ground for 15 min. The obtained mixture was placed in a stainless steel jar along with stainless steel balls, in which the ball-to-powder ratio was 30:1 in weight. The mixture was ball-milled for 7 h to form SnP_3. For the synthesis of the SnP_3/C composite, additional ball milling for 3 h was carried out using the mixture of the synthesized SnP_3 powder and amorphous carbon (Super P, Timcal) in a weight ratio of 80:20.

Material Characterization. The crystal structures of the synthesized SnP_3 and SnP_3/C nanocomposites were characterized using XRD (D/MAX Ultima III, Rigaku) with a Cu Kα source (2 kW, max 60 kV, and 55 mA). The surface morphology and microstructure of the sample were obtained using SEM (S-4700/EX-200, Hitachi) at an acceleration voltage of 10 kV and TEM (JEM-2100F, JEOL). The presence of carbon in the SnP_3/C nanocomposite was identified by Raman spectroscopy (NRS-5100, JASCO). The N_2 adsorption−desorption isotherm for the synthesized materials was analyzed using a BET analyzer (ASAP 2020, Micromerities). In addition, the surface chemical structure of the materials was characterized by XPS (Multilab 2000, VG).

Electrochemical Characterization. The synthesized pristine SnP_3 and SnP_3/C-active material were mixed with Super C65 carbon as a conductive agent and polyacrylate as a binder in a weight ratio of 7:2:1 and 8:1:1, respectively. *N*-methyl-2-pyrrolidone solvent was used to create a homogeneous slurry. Then, the slurry was cast onto a Cu foil, followed by drying at 85 °C overnight in a vacuum oven. The

DOI: 10.1021/acsami.9b08088
ACS Appl. Mater. Interfaces 2019, 11, 26976−26984

electrodes were punched into 14 mm diameter disks. Using a 2032 type coin cell, the pristine SnP_3 or SnP_3/C working electrode was assembled with K-metal as a counter/reference electrode and a glass fiber separator (Whatman) soaked with 0.75 M KPF_6 in ethylene carbonate and diethyl carbonate (1:1, by volume), in an Ar-filled glovebox. The mass loading of the electrode was controlled at approximately 0.6−1.0 mg cm^{-2}. The working electrode was discharged and charged in the potential range of 0.01−2 V vs K^+/K using the battery cycler (WonATech-WBCS 3000). In addition, the full cell was composed of an SnP_3/C anode, a potassium Prussian blue ($KFe_2(CN_6)$) cathode, and the same electrolyte, in which the cathode-to-anode mass loading ratio was 4:1. Galvanostatic charge and discharge tests were carried out in a cell potential range of 0.5−3.8 V. In addition, the EIS of the half cells was measured through potentiostat/EIS (Gamry-PC750) at a frequency range of 10 mHz to 100 kHz.

■ ASSOCIATED CONTENT

Supporting Information

The Supporting Information is available free of charge on the ACS Publications website at DOI: 10.1021/acsami.9b08088.

Figure S1: N2 adsorption/desorption isotherms,Figure S2: Galvanostatic discharge-charge profile, Figure S3: SEM images, Figure S4: Selected discharge-charge potential profiles, Figure S5: XRD patterns of the discharged electrode, Figure S6: TEM images, Figure S7: XPS analysis, and Figure S8: XRD pattern of potassium Prussian blue (PDF)

■ AUTHOR INFORMATION

Corresponding Authors

*E-mail: gzcao@uw.edu.

*E-mail: parkcj@jnu.ac.kr. Tel: +(82)-62-530-1704. Fax: +(82)-62-530-1699 (C.-J.P.).

ORCID

Chan-Jin Park: 0000-0002-3993-1908

Notes

The authors declare no competing financial interest.

■ ACKNOWLEDGMENTS

This work was supported by the National Research Foundation of Korea (NRF) grant funded by the Korea government (MSIT) (No. 2018R1A5A1025224) and by the Korea Institute of Energy Technology Evaluation and Planning (KETEP) grant funded by the MOTIE, Korea (No. 20172420108730).

■ REFERENCES

(1) Wessells, C. D.; Peddada, S. V.; Huggins, R. A.; Cui, Y. Nickel Hexacyanoferrate Nanoparticle Electrodes for Aqueous Sodium and Potassium Ion Batteries. *Nano Lett.* **2011**, *11*, 5421−5425.

(2) Beltrop, K.; Beuker, S.; Heckmann, A.; Winter, M.; Placke, T. Alternative Electrochemical Energy Storage: Potassium-Based Dual-Graphite Batteries. *Energy Environ. Sci.* **2017**, *10*, 2090−2094.

(3) Eftekhari, A.; Jian, Z.; Ji, X. Potassium Secondary Batteries. *ACS Appl. Mater. Interfaces* **2017**, *9*, 4404−4419.

(4) Zhang, W.; Liu, Y.; Guo, Z. Approaching high-performance potassium-ion batteries via advanced design strategies and engineering. *Sci. Adv.* **2019**, *5*, No. eaav7412.

(5) Okoshi, M.; Yamada, Y.; Komaba, S.; Yamada, A.; Nakai, H. Theoretical Analysis of Interactions between Potassium Ions and Organic Electrolyte Solvents: A Comparison with Lithium, Sodium, and Magnesium Ions. *J. Electrochem. Soc.* **2017**, *164*, A54−A60.

(6) McCulloch, W. D.; Ren, X.; Yu, M.; Huang, Z.; Wu, Y. Potassium-Ion Oxygen Battery Based on a High Capacity Antimony Anode. *ACS Appl. Mater. Interfaces* **2015**, *7*, 26158−26166.

(7) Wu, X.; Leonard, D. P.; Ji, X. Emerging Non-Aqueous Potassium-Ion Batteries: Challenges and Opportunities. *Chem. Mater.* **2017**, *29*, 5031−5042.

(8) Fan, L.; Chen, S.; Ma, R.; Wang, J.; Wang, L.; Zhang, Q.; Zhang, E.; Liu, Z.; Lu, B. Ultrastable Potassium Storage Performance Realized by Highly Effective Solid Electrolyte Interphase Layer. *Small* **2018**, *14*, No. 1801806.

(9) Zhang, C.; Xu, Y.; Zhou, M.; Liang, L.; Dong, H.; Wu, M.; Yang, Y.; Lei, Y. Potassium Prussian Blue Nanoparticles: A Low-Cost Cathode Material for Potassium-Ion Batteries. *Adv. Funct. Mater.* **2017**, *27*, No. 1604307.

(10) Bie, X.; Kubota, K.; Hosaka, T.; Chihara, K.; Komaba, S. A Novel K-ion Battery: Hexacyanoferrate(II)/Graphite Cell. *J. Mater. Chem. A* **2017**, *5*, 4325−4330.

(11) Eftekhari, A. Potassium Secondary Cell Based on Prussian Blue Cathode. *J. Power Sources* **2004**, *126*, 221−228.

(12) Chihara, K.; Katogi, A.; Kubota, K.; Komaba, S. $KVPO_4F$ and $KVOPO_4$ Toward 4 Volt-Class Potassium-Ion Batteries. *Chem. Commun.* **2017**, *53*, 5208−5211.

(13) Recham, N.; Rousse, G.; Sougrati, M. T.; Chotard, J. N.; Frayret, C.; Mariyappan, S.; Melot, B. C.; Jumas, J. C.; Tarascon, J. M. Preparation and Characterization of a Stable $FeSO_4F$-Based Framework for Alkali Ion Insertion Electrodes. *Chem. Mater.* **2012**, *24*, 4363−4370.

(14) Vaalma, C.; Giffin, G. A.; Buchholz, D.; Passerini, S. Non-Aqueous K-Ion Battery Based on Layered $K_{0.3}MnO_2$ and Hard Carbon/Carbon Black. *J. Electrochem. Soc.* **2016**, *163*, A1295−A1299.

(15) Hironaka, Y.; Kubota, K.; Komaba, S. P2- and P3-K_xCoO_2 as an Electrochemical Potassium Intercalation Host. *Chem. Commun.* **2017**, *53*, 3693−3696.

(16) Deng, T.; Fan, X.; Luo, C.; Chen, J.; Chen, L.; Hou, S.; Eidson, N.; Zhou, X.; Wang, C. Self-templated Formation of P2-type $K_{0.6}CoO_2$ Microspheres for High Reversible Potassium-ion Batteries. *Nano Lett.* **2018**, *18*, 1522−1529.

(17) Han, J.; Li, G. N.; Liu, F.; Wang, M.; Zhang, Y.; Hu, L.; Dai, C.; Xu, M. Investigation of $K_3V_2(PO_4)_3$/C Nanocomposites as High-Potential Cathode Materials for Potassium Ion Batteries. *Chem. Commun.* **2017**, *53*, 1805−1808.

(18) Mathew, V.; Kim, S.; Kang, J.; Gim, J.; Song, J.; Baboo, J. P.; Park, W.; Ahn, D.; Han, J.; Gu, L.; Wang, Y.; Hu, Y. S.; Sun, Y. K.; Kim, J. Amorphous Iron Phosphate: Potential Host for Various Charge Carrier Ions. *NPG Asia Mater.* **2014**, *6*, No. e138.

(19) Deng, T.; Fan, X.; Chen, J.; Chen, L.; Luo, C.; Zhou, X.; Yang, J.; Zheng, S.; Wang, C. Layered P2-Type $K_{0.65}Fe_{0.5}Mn_{0.5}O_2$ Microspheres as Superior Cathode for High-Energy Potassium-Ion Batteries. *Adv. Funct. Mater.* **2018**, *28*, No. 1800219.

(20) Chen, Y.; Luo, W.; Carter, M.; Zhou, L.; Dai, J.; Fu, K.; Lacey, S.; Li, T.; Wan, J.; Han, X.; Bao, Y.; Hu, L. Organic Electrode for Non-Aqueous Potassium-Ion Batteries. *Nano Energy* **2015**, *18*, 205−211.

(21) Fan, L.; Liu, Q.; Chen, S.; Lin, K.; Xu, Z.; Lu, B. Potassium-Based Dual Ion Battery with Dual-Graphite Electrode. *Small* **2017**, *13*, No. 1701011.

(22) Zhang, W.; Mao, J.; Li, S.; Chen, Z.; Guo, Z. Phosphorus-Based Alloy Materials for Advanced Potassium-Ion Battery Anode. *J. Am. Chem. Soc.* **2017**, *139*, 3316−3319.

(23) Xie, Y.; Chen, Y.; Liu, L.; Tao, P.; Fan, M.; Xu, N.; Shen, X.; Yan, C. Ultra-High Pyridinic N-Doped Porous Carbon Monolith Enabling High-Capacity K-Ion Battery Anodes for Both Half-Cell and Full-Cell Applications. *Adv. Mater.* **2017**, *29*, No. 1702268.

(24) Huang, K.; Xing, Z.; Wang, L.; Wu, X.; Zhao, W.; Qi, X.; Wang, H.; Ju, Z. Direct Synthesis of 3D Hierarchically Porous Carbon/Sn Composites via in Situ Generated NaCl Crystals as Templates for Potassium-Ion Batteries Anode. *J. Mater. Chem. A* **2018**, *6*, 434−442.

(25) Wu, Y.; Hu, S.; Xu, R.; Wang, J.; Peng, Z.; Zhang, Q.; Yu, Y. Boosting Potassium-Ion Battery Performance by Encapsulating Red

Phosphorus in Free-Standing Nitrogen-Doped Porous Hollow Carbon Nanofibers. *Nano Lett.* **2019**, *19*, 1351−1358.
(26) Xiong, P.; Bai, P.; Tu, S.; Cheng, M.; Zhang, J.; Sun, J.; Xu, Y. Red Phosphorus Nanoparticle@3D Interconnected Carbon Nanosheet Framework Composite for Potassium-Ion Battery Anodes. *Small* **2018**, *14*, No. 1802140.
(27) Sultana, I.; Ramireddy, T.; Rahman, M. M.; Chen, Y.; Glushenkov, A. M. Tin-Based Composite Anodes for Potassium-Ion Batteries. *Chem. Commun.* **2016**, *52*, 9279−9282.
(28) Lei, K.; Wang, C.; Liu, L.; Luo, Y.; Mu, C.; Li, F.; Chen, J. A Porous Network of Bismuth Used as Anode Material for High-Energy-Density Potassium-Ion Batteries. *Angew. Chem.* **2018**, *130*, 4777−4781.
(29) Yi, Z.; Lin, N.; Zhang, W.; Wang, W.; Zhu, Y.; Qian, Y. Preparation of Sb Nanoparticles in Molten Salt and Their Potassium Storage Performance and Mechanism. *Nanoscale* **2018**, *10*, 13236−13241.
(30) Kim, Y.; Kim, Y.; Choi, A.; Woo, S.; Mok, D.; Choi, N. S.; Jung, Y. S.; Ryu, J. H.; Oh, S. M.; Lee, K. T. Tin Phosphide as a Promising Anode Material for Na-Ion Batteries. *Adv. Mater.* **2014**, *26*, 4139−4144.
(31) Liu, J.; Kopold, P.; Wu, C.; Van Aken, P. A.; Maier, J.; Yu, Y. Uniform Yolk−Shell Sn_4P_3@C Nanospheres as High-Capacity and Cycle-Stable Anode Materials for Sodium-Ion Batteries. *Energy Environ. Sci.* **2015**, *8*, 3531−3538.
(32) Fullenwarth, J.; Darwiche, A.; Soares, A.; Donnadieu, B.; Monconduit, L. NiP_3: A Promising Negative Electrode for Li- and Na-Ion Batteries. *J. Mater. Chem. A* **2014**, *2*, 2050−2059.
(33) Xu, Y.; Peng, B.; Mulder, F. M. A High-Rate and Ultrastable Sodium Ion Anode Based on a Novel Sn_4P_3-P@Graphene Nanocomposite. *Adv. Energy Mater.* **2018**, *8*, No. 1701847.
(34) Fan, X.; Mao, J.; Zhu, Y.; Luo, C.; Suo, L.; Gao, T.; Han, F.; Liou, S. C.; Wang, C. Superior Stable Self-Healing SnP_3 Anode for Sodium-Ion Batteries. *Adv. Energy Mater.* **2015**, *5*, No. 1500174.
(35) Li, W.; Chou, S.-L.; Wang, J.-Z.; Kim, J. H.; Liu, H.-K.; Dou, S.-X. $Sn_{4+x}P_3$@ Amorphous Sn-P Composites as Anodes for Sodium-Ion Batteries with Low Cost, High Capacity, Long Life, and Superior Rate Capability. *Adv. Mater.* **2014**, *26*, 4037.
(36) Kim, S. O.; Manthiram, A. The Facile Synthesis and Enhanced Sodium-Storage Performance of a Chemically Bonded CuP_2/C Hybrid Anode. *Chem. Commun.* **2016**, *52*, 4337−4340.
(37) Qi, W.; Zhao, H.; Wu, Y.; Zeng, H.; Tao, T.; Chen, C.; Kuang, C.; Zhou, S.; Huang, Y. Facile Synthesis of Layer Structured GeP_3/C with Stable Chemical Bonding for Enhanced Lithium-Ion Storage. *Sci. Rep.* **2017**, *7*, No. 43582.
(38) Su, F.; Poh, C. K.; Chen, J. S.; Xu, G.; Wang, D.; Li, Q.; Lin, J.; Lou, X. W. Nitrogen-Containing Microporous Carbon Nanospheres with Improved Capacitive Properties. *Energy Environ. Sci.* **2011**, *4*, 717−724.
(39) Huang, J.; Lin, X.; Tan, H.; Zhang, B. Bismuth Microparticles as Advanced Anodes for Potassium-Ion Battery. *Adv. Energy Mater.* **2018**, *8*, No. 1703496.
(40) Gao, H.; Zhou, T.; Zheng, Y.; Zhang, Q.; Liu, Y.; Chen, J.; Liu, H.; Guo, Z. CoS Quantum Dot Nanoclusters for High-Energy Potassium-Ion Batteries. *Adv. Funct. Mater.* **2017**, *27*, No. 1702634.
(41) Deng, L.; Yang, Z.; Tan, L.; Zeng, L.; Zhu, Y.; Guo, L. Investigation of the Prussian Blue Analog $Co_3[Co(CN)_6]_2$ as an Anode Material for Nonaqueous Potassium-Ion Batteries. *Adv. Mater.* **2018**, *30*, No. 1802510.
(42) Li, P.; Hwang, J.-Y.; Park, S.-M.; Sun, Y.-K. Superior Lithium/Potassium Storage Capability of Nitrogen-Rich Porous Carbon Nanosheets Derived from Petroleum Coke. *J. Mater. Chem. A* **2018**, *6*, 12551−12558.
(43) Qi, X.; Huang, K.; Wu, X.; Zhao, W.; Wang, H.; Zhuang, Q.; Ju, Z. Novel Fabrication of N-doped Hierarchically Porous Carbon with Exceptional Potassium Storage Properties. *Carbon* **2018**, *131*, 79−85.
(44) Xiong, P.; Zhao, X.; Xu, Y. Nitrogen-Doped Carbon Nanotubes Derived from Metal−Organic Frameworks for Potassium-Ion Battery Anodes. *ChemSusChem* **2018**, *11*, 202−208.
(45) Zhao, X.; Tang, Y.; Ni, C.; Wang, J.; Star, A.; Xu, Y. Free-Standing Nitrogen-Doped Cup-Stacked Carbon Nanotube Mats for Potassium-Ion Battery Anodes. *ACS Appl. Energy Mater.* **2018**, *1*, 1703−1707.
(46) Chen, M.; Wang, W.; Liang, X.; Gong, S.; Liu, J.; Wang, Q.; Guo, S.; Yang, C. Sulfur/Oxygen Codoped Porous Hard Carbon Microspheres for High-Performance Potassium-Ion Batteries. *Adv. Energy Mater.* **2018**, No. 1800171.
(47) Han, J.; Xu, M.; Niu, Y.; Li, G.-N.; Wang, M.; Zhang, Y.; Jia, M.; Li, C. M. Exploration of $K_2Ti_8O_{17}$ as an Anode Material for Potassium-Ion Batteries. *Chem. Commun.* **2016**, *52*, 11274−11276.
(48) Zhang, W.; Pang, W. K.; Sencadas, V.; Guo, Z. Understanding High-Energy-Density Sn_4P_3 Anodes for Potassium-Ion Batteries. *Joule* **2018**, 1534−1547.
(49) Ren, X.; Zhao, Q.; McCulloch, W. D.; Wu, Y. MoS_2 as a Long-Life Host Material for Potassium Ion Intercalation. *Nano Res.* **2017**, *10*, 1313−1321.
(50) Lakshmi, V.; Chen, Y.; Mikhaylov, A. A.; Medvedev, A. G.; Sultana, I.; Rahman, M. M.; Lev, O.; Prikhodchenko, P. V.; Glushenkov, A. M. Nanocrystalline SnS_2 Coated onto Reduced Graphene Oxide: Demonstrating the Feasibility of a Non-Graphitic Anode with Sulfide Chemistry for Potassium-ion Batteries. *Chem. Commun.* **2017**, *53*, 8272−8275.
(51) Sultana, I.; Rahman, M. M.; Mateti, S.; Ahmadabadi, V. G.; Glushenkov, A. M.; Chen, Y. K-ion and Na-ion Storage Performances of Co_3O_4−Fe_2O_3 Nanoparticle-Decorated Super P Carbon Black Prepared by a Ball Milling Process. *Nanoscale* **2017**, *9*, 3646−3654.
(52) Share, K.; Cohn, A. P.; Carter, R.; Rogers, B.; Pint, C. L. Role of Nitrogen-Doped Graphene for Improved High-Capacity Potassium Ion Battery Anodes. *ACS Nano* **2016**, *10*, 9738−9744.
(53) Kundu, D.; Talaie, E.; Duffort, V.; Nazar, L. F. The Emerging Chemistry of Sodium Ion Batteries for Electrochemical Energy Storage. *Angew. Chem., Int. Ed.* **2015**, *54*, 3432−3448.

DOI: 10.1021/acsami.9b08088
ACS Appl. Mater. Interfaces 2019, 11, 26976−26984